Supplementary Information

Stretchable thermogalvanic hydrogel thermocell with record-high specific output power density enabled by ion-induced crystallization

*Ding Zhang, Yin Mao, Fei Ye, Qi Li, Peijia Bai, Wen He, Rujun Ma**

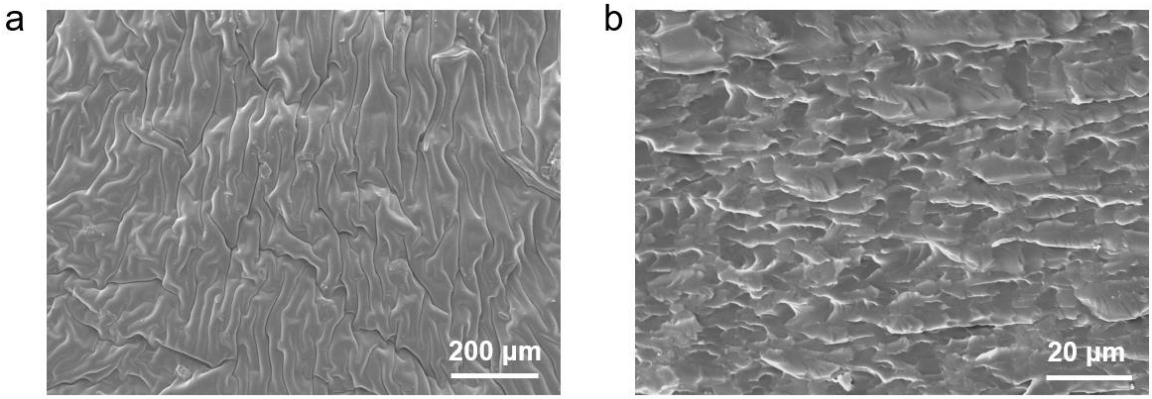

Fig. S1. SEM characterization of the PAAm-SA hydrogel. (a,b) The surface (a) and cross-section (b) images of the PAAm-SA hydrogel.

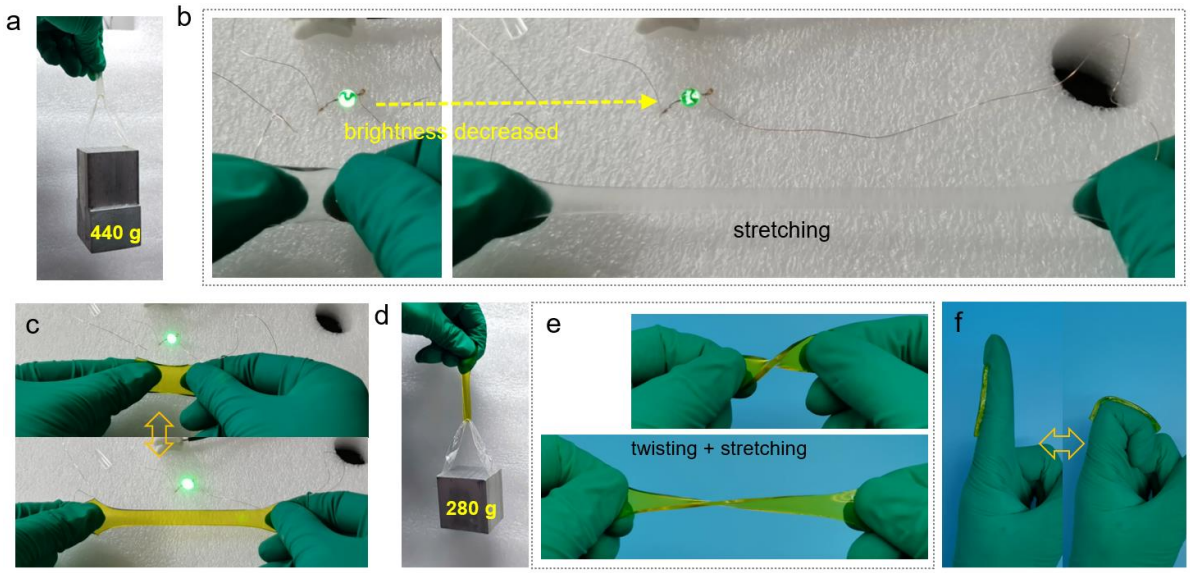

Fig. S2. The mechanical performance analysis of the PAAm-SA hydrogel. (a) The optical image of the hydrogel supporting a heavy Al block. (b) The brightness change of a LED with the hydrogel as a conducting wire at different stretched strains. (c) The brightness change of a LED with the hydrogel soaked into $[Fe(CN)_6]^{3-/4-}$ solution, indicating the excellent conductivity of the soaked hydrogel. (d) The optical image of an Al block supported by a soaked hydrogel. (e,f) The measurement for excellent torsional and tensile performance (e) and adhesion property (f) of the soaked hydrogel.

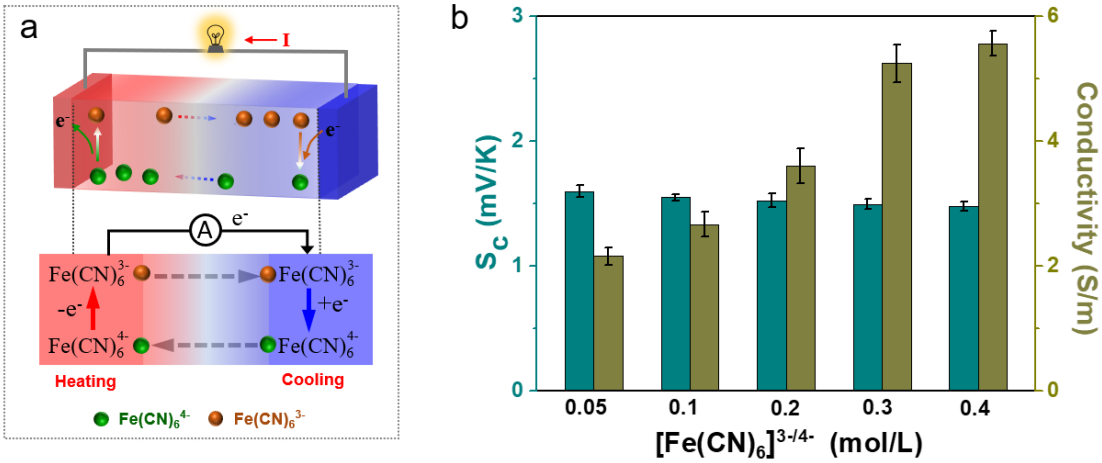

Fig. S3. (a) The schematic diagram of the working mechanism based on thermogalvanic effect. (b) The thermopower and conductivity change of the STHTC with 0.05-0.4 mol/L $[Fe(CN)_6]^{3-/4-}$.

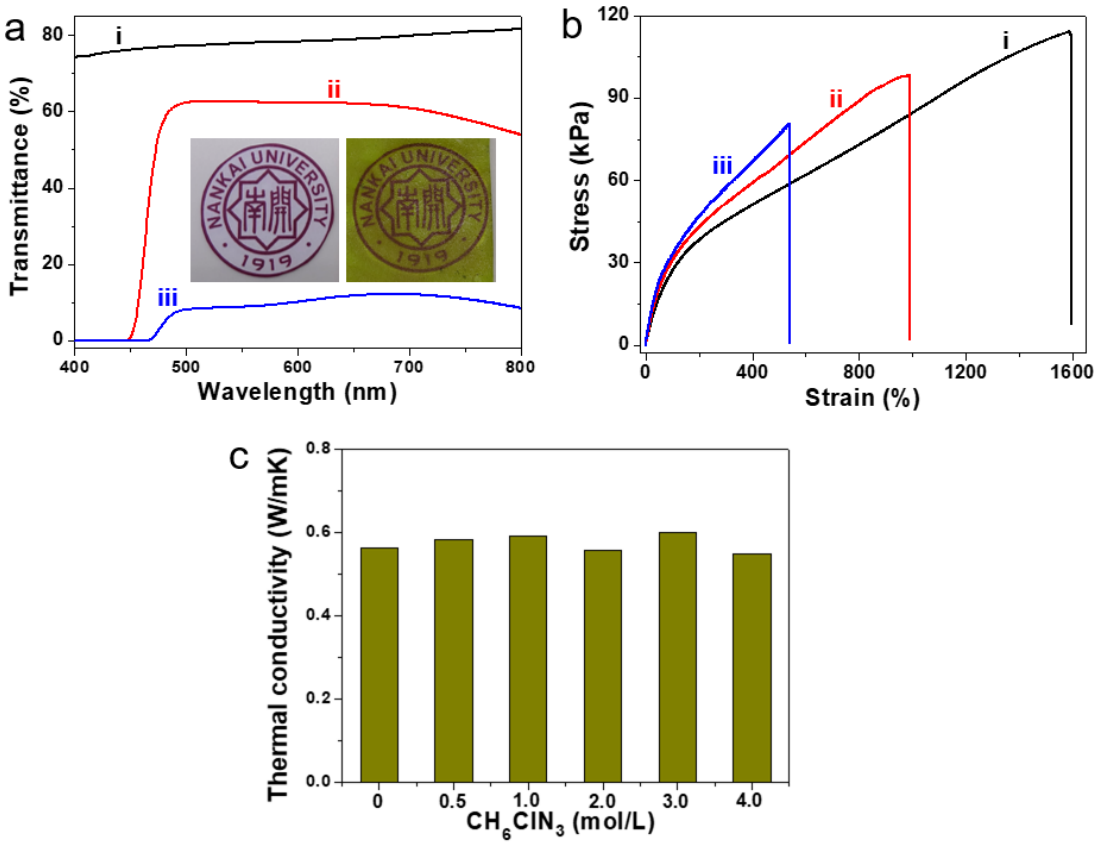

Fig. S4. The performance comparison of different PAAm-SA hydrogels. (a,b) The transmittance (a) and stretchability (b) comparison of different PAAm-SA hydrogels. (c) The variation of the thermal conductivity of the PAAm-SA hydrogel with 0-4.0 mol/L CH_6ClN_3 and 0.3 mol/L $[Fe(CN)_6]^{3-/4-}$ as different soaking solutions.

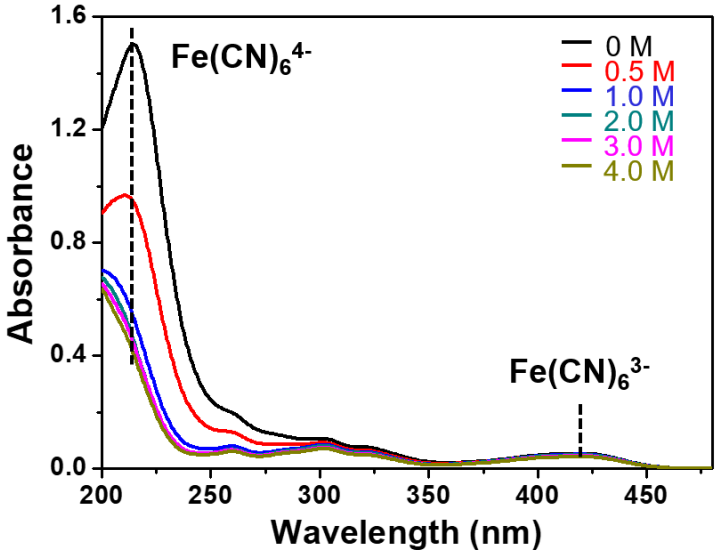

Fig. S5. The UV-Vis absorbance spectra change of the soaked solution with 0-4.0 mol/L CH_6ClN_3 and 0.3 mol/L $[Fe(CN)_6]^{3-/4-}$.

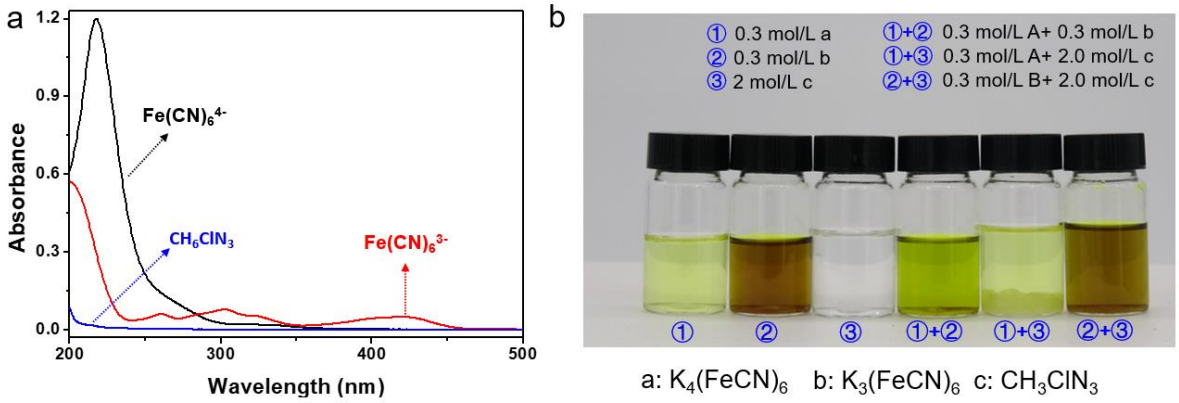

Fig. S6. (a) The comparison of three individual UV-Vis absorbance spectra corresponding to $K_4Fe(CN)_6$, $K_3Fe(CN)_6$ and CH_6ClN_3. (b) The dissolution situations of the soaking solution with different combinations among $K_4Fe(CN)_6$, $K_3Fe(CN)_6$ and CH_6ClN_3.

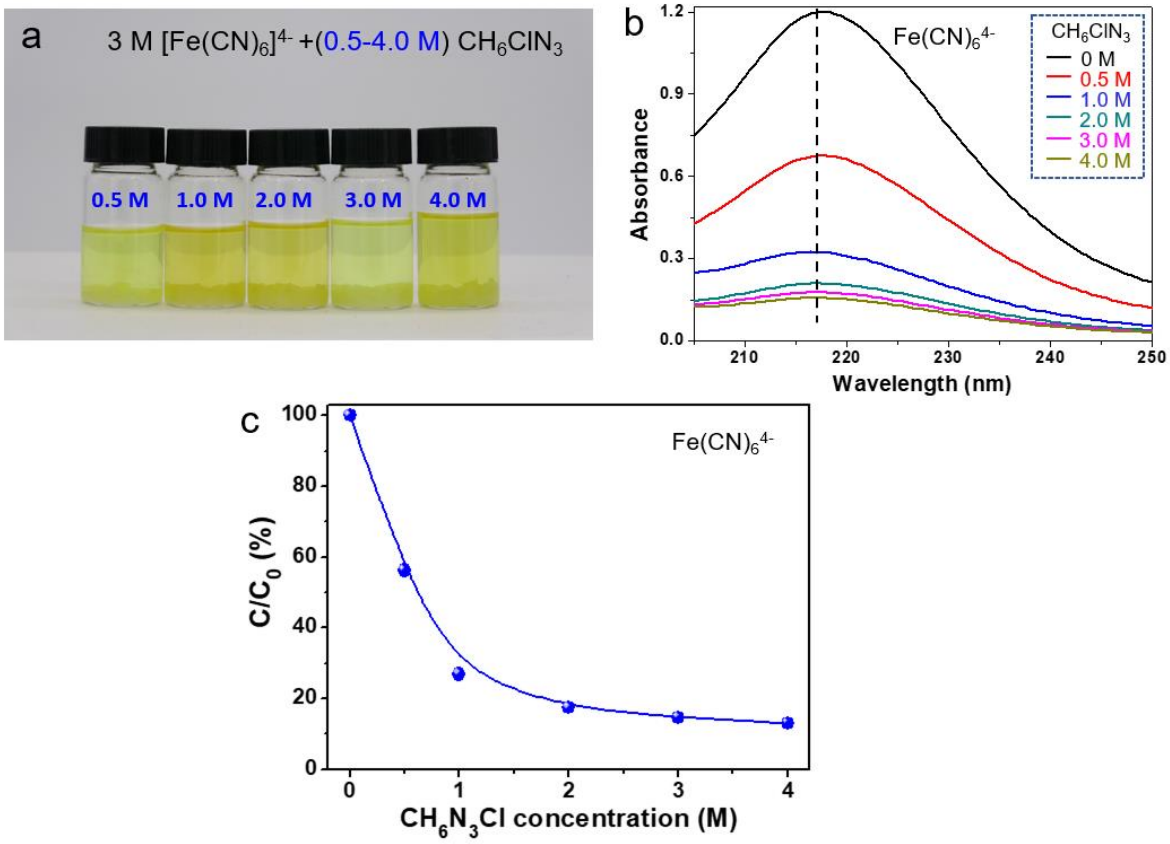

Fig. S7. The dissolution comparison of the solutions containing $K_4Fe(CN)_6$ and CH_6ClN_3. (a-c) The optical images (a), UV-Vis absorbance spectra (b), and the relative concentration change (c) of $[Fe(CN)_6]^{4-}$ in the solution with 3 mol/L $K_4Fe(CN)_6$ and 0.5-4.0 mol/L CH_6ClN_3.

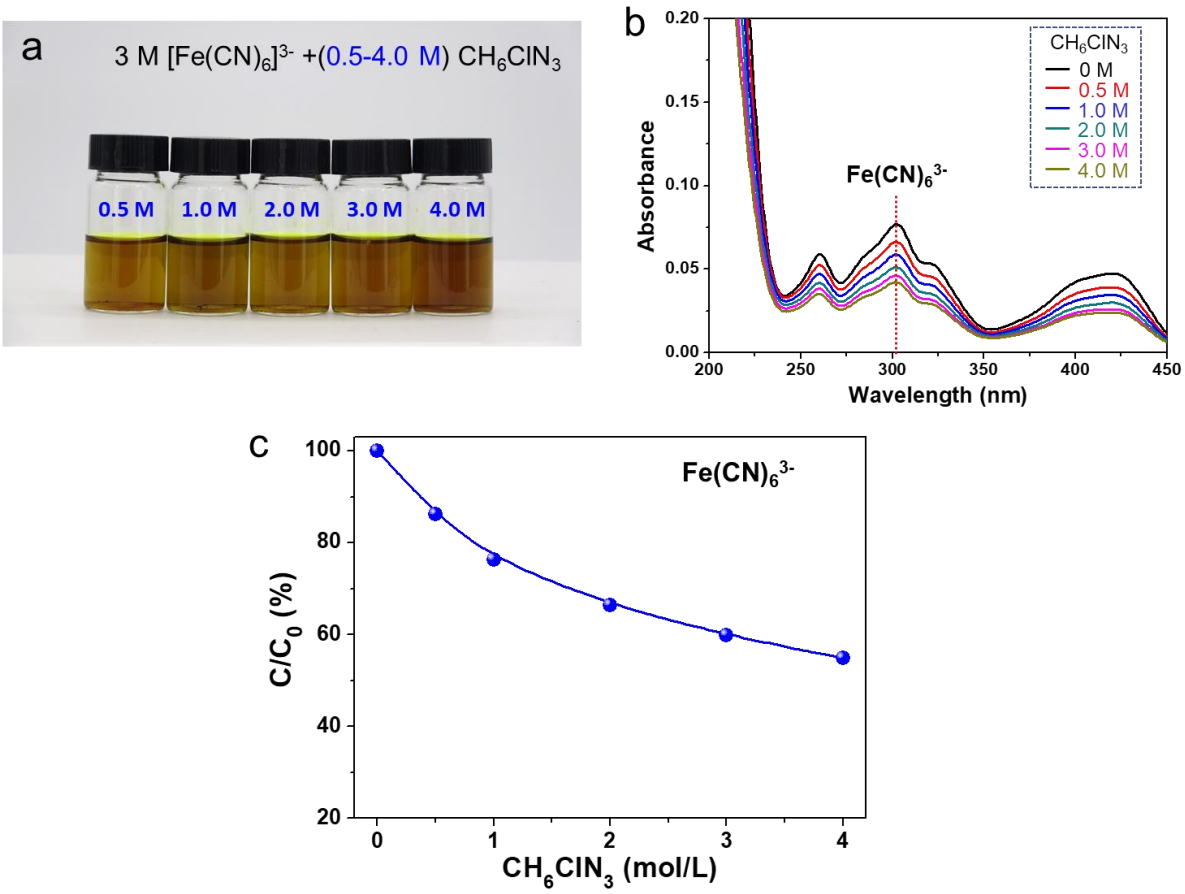

Fig. S8. The dissolution comparison of the solutions containing $K_3Fe(CN)_6$ and CH_6ClN_3. (a-c) The optical images (a), UV-Vis absorbance spectra (b), and the relative concentration change (c) of $[Fe(CN)_6]^{3-}$ in the solution with 3 mol/L $K_3Fe(CN)_6$ and 0.5-4.0 mol/L CH_6ClN_3.

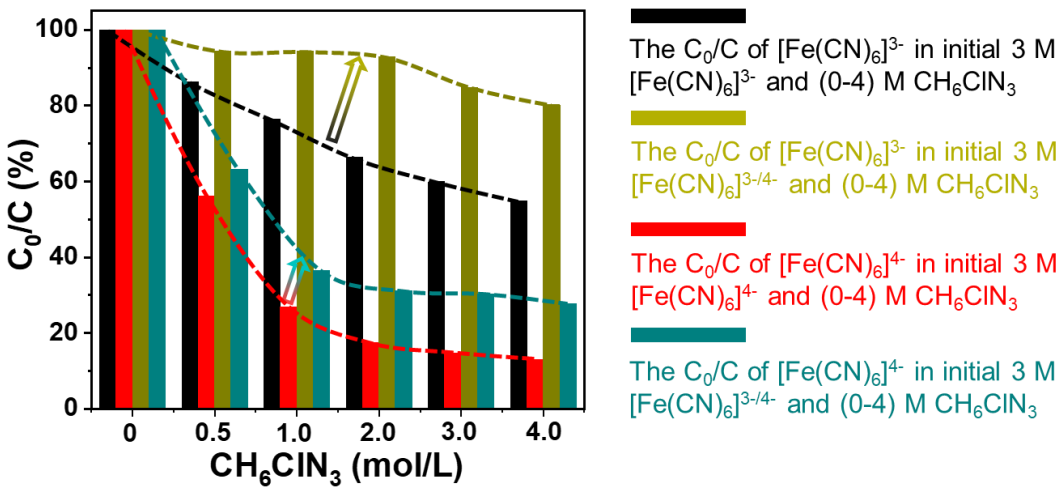

Fig. S9. The relative concentration change of $[Fe(CN)_6]^{3-}$ and $[Fe(CN)_6]^{4-}$ in different initial solutions.

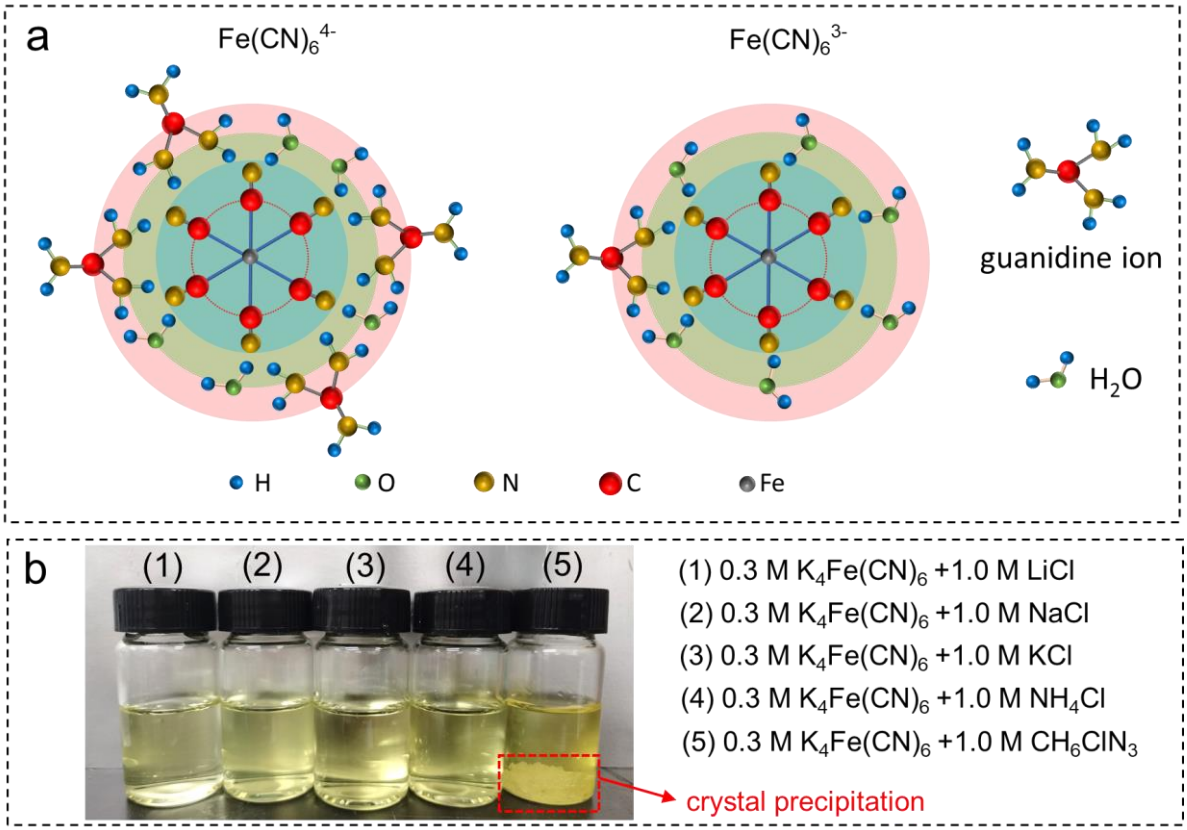

Fig. S10 (a) The schematic diagram of solvation situations of $[Fe(CN)_6]^{3-/4-}$ in CH_6ClN_3 solution. (b) The comparison of the effect of other species on the crystallization of $[Fe(CN)_6]^{4-}$ ion.

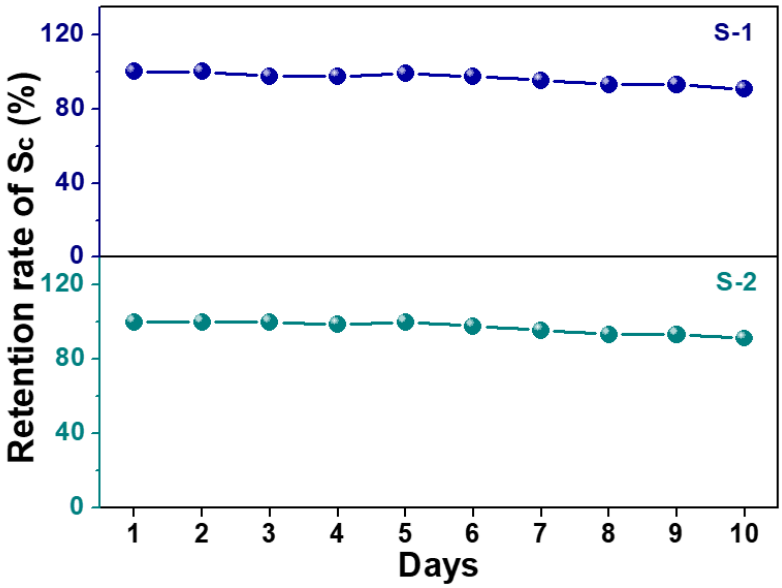

Fig. S11. The thermopower retention rate of two STHTCs after being wrapped in a cling film and placed in the air for 10 days.

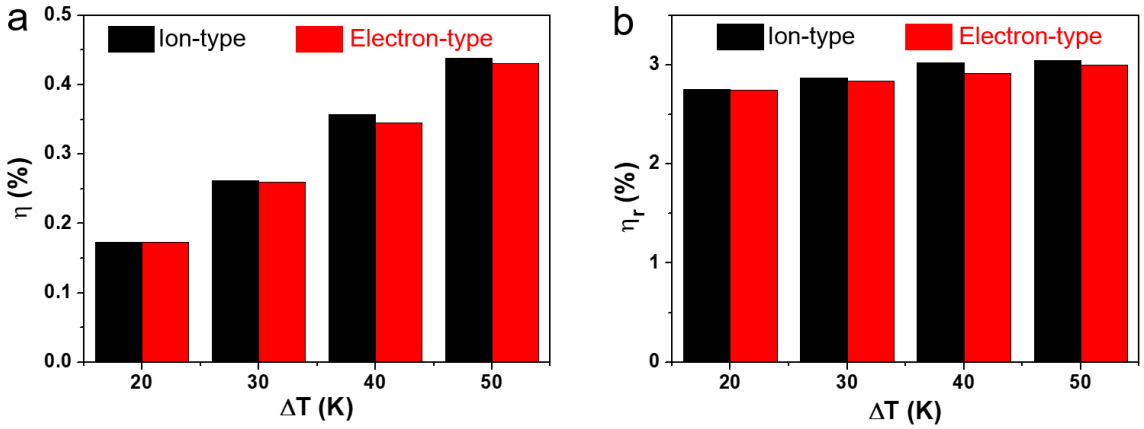

Fig. S12. The comparison of thermal conversion efficiency calculated by ion-type and electron-type methods. (a,b) The comparison of thermal energy conversion efficiency (a) and Carnot-relative efficiency (b) of the STHTC under different ΔT.

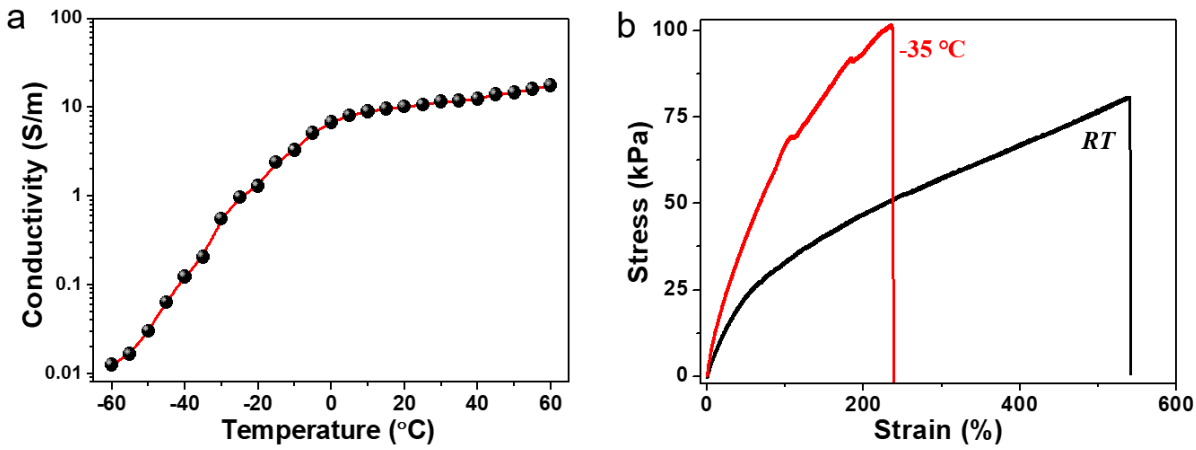

Fig. S13. The performance measure of the STHTC at low-temperature. (a) The conductivity changes of the STHTC under a large temperature span between -60 to 60 °C. (b) The comparison of the stress-strain curves of the STHTC under an ultra-low cold (-35 °C) environment and room temperature (*RT*).

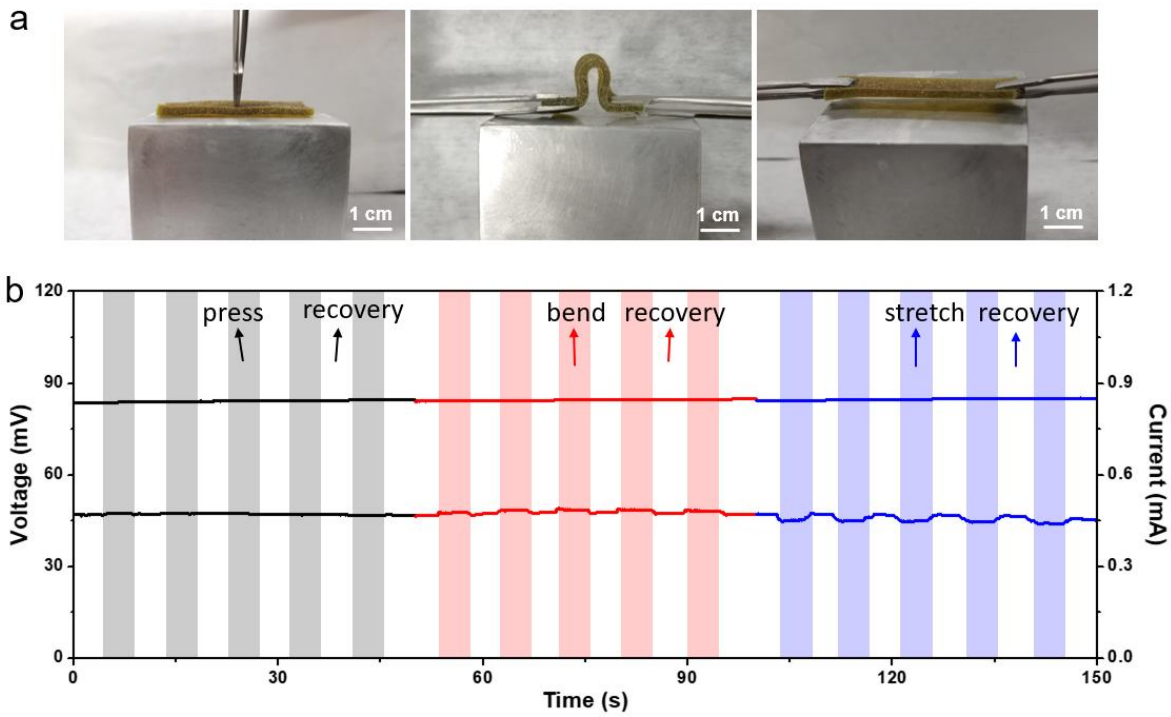

Fig. S14. The stability measure of the STHTC at three groups of small deformation operations. (a,b) The optical images of the STHTC being periodically pressed, bent, and stretched (a) and corresponding electrical output change (b).

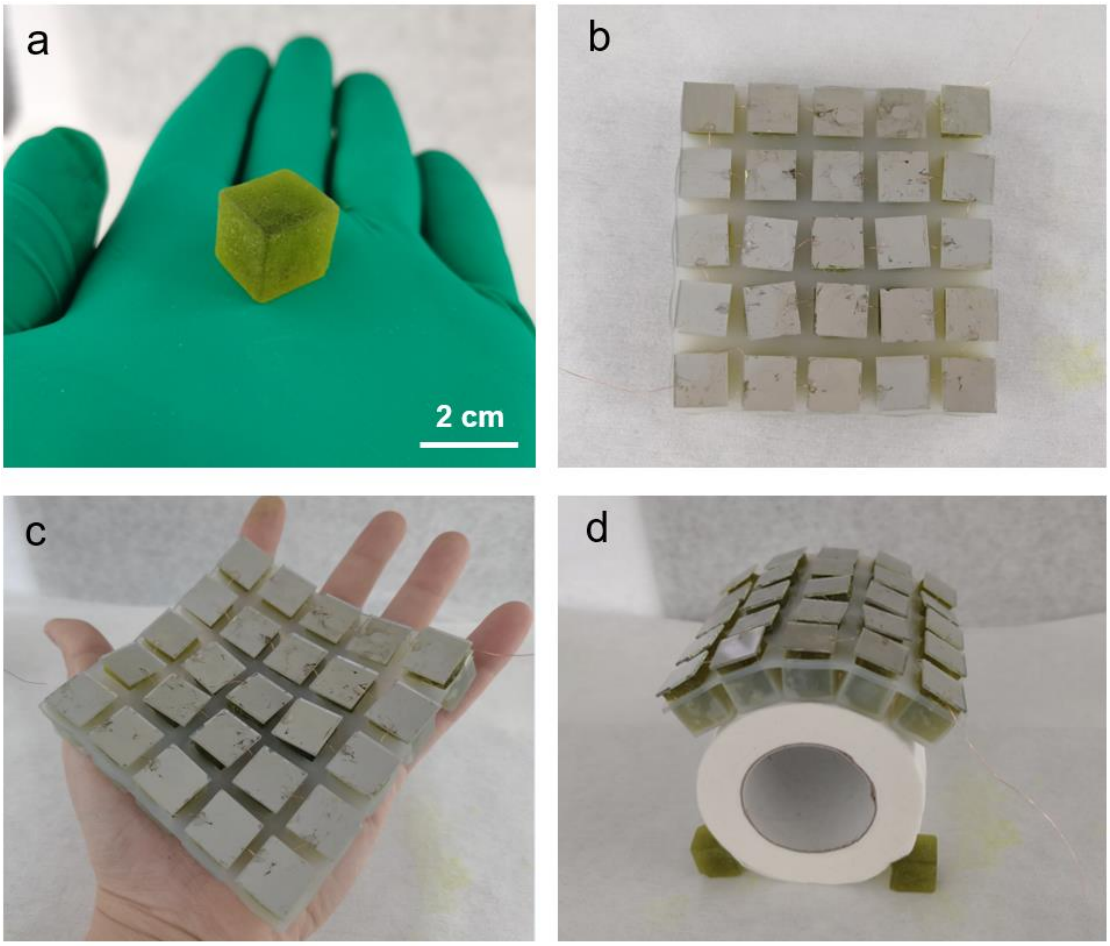

Fig. S15. The cubic STHTC block and the 5×5 STHTC array device. (a) Optical images of cubic STHTC. (b-d) Optical images of fabricated 5×5 STHTC array device (b), showing good flexibility (c) and bendability (d).

Supplementary Note

Note S1:

With the increase of CH_6ClN_3 from 0.5 to 2.0 mol/L, the concentration of $[Fe(CN)_6]^{4-}$ quickly decreases while the concentration of $[Fe(CN)_6]^{3-}$ decreased slightly (**Fig. 2**b), which will promote the reversible redox, thus increasing the S_c. Meanwhile, the Cl^- ions from CH_6ClN_3 can increase the electrical conductivity to a certain extent. When the CH_6ClN_3 increases over 2.0 mol/L, there is a relatively large concentration reduction for $[Fe(CN)_6]^{3-}$ than $[Fe(CN)_6]^{4-}$. The reduction of $[Fe(CN)_6]^{3-}$ will inhibit the redox and decrease the S_c slightly (**Fig. 2**b). At the same time, the increase of crystalline precipitate may hinder the ions transport, thus reducing the conductivity.[1]

Note S2:

For the STHTC, the Power Factor (*PF*) and Figure of merit (*ZT*) can be calculated according to the calculation method for the traditional thermoelectrical materials, which can be expressed as[2,3]:

$$PF = \alpha^2\sigma \quad (1)$$

$$ZT = \alpha^2\sigma T/\kappa \quad (2)$$

Where the α, σ, T, κ are the seebeck coefficient, electrical conductivity, Kelvin temperature, and thermal conductivity. Owing to the appearance of the ΔT, there is a temperature gradient across the STHTC, therefore the average *ZT* can be changed as:

$$ZT_{average} = \alpha^2\sigma(T_c+T_h)/2\kappa \quad (3)$$

The thermal conversion efficiency (η) of the traditional thermoelectrical materials can be expressed as[4,5]:

$$\eta = \frac{\Delta T}{T}\frac{\sqrt{1+ZT}-1}{\sqrt{1+ZT}+\frac{T_c}{T_h}} \quad (4)$$

Where the ΔT, T, ZT, T_c, T_h are the temperature difference, Kelvin temperature, Figure of merit, cold side temperature and hot side temperature, respectively.

References:

[1] Y. Horowitz, M. Lifshitz, A. Greenbaum, Y. Feldman, D. Golodnitsky. Review-Polymer/Ceramic Interface Barriers: The Fundamental Challenge for Advancing Composite Solid Electrolytes for Li-Ion Batteries. *J. Electrochem. Soc.* 2020, **167**, 160514.

[2] X.-L. Shi, J. Zou, Z.-G. Chen. Advanced Thermoelectric Design: From Materials and Structures to Devices. *Chem. Rev.* 2020, **120**, 7399.

[3] L. Yang, Z.-G. Chen, M. S. Dargusch, J. Zou. High Performance Thermoelectric Materials: Progress and Their Applications. *Adv. Energy Mater.* 2018, **8**, 1701797.

[4] Q. Yan, M. G. Kanatzidis. High-performance thermoelectrics and challenges for practical devices. *Nat. Mater.* 2021, **21**, 503.

[5] H. Zhu, R. He, J. Mao, Q. Zhu, C. Li, J. Sun, W. Ren, Y. Wang, Z. Liu, Z. Tang.Discovery of ZrCoBi based half Heuslers with high thermoelectric conversion efficiency. *Nat. Commun.* 2018, **9**, 2497.